Journal of Power Sources 615 (2024) 235070

Contents lists available at ScienceDirect

Journal of Power Sources

journal homepage: www.elsevier.com/locate/jpowsour

Capabilities of a novel electrochemical cell for *operando* XAS and SAXS investigations for PEM fuel cells and water electrolysers

Marco Bogar [a,*], Yurii Yakovlev [b], Simone Pollastri [c,d], Roberto Biagi [c,e,f], Heinz Amenitsch [g], Rodolfo Taccani [a], Iva Matolínová [b]

[a] Department of Engineering and Architecture, University of Trieste, Via Alfonso Valerio 6/1, 34127, Trieste, Italy
[b] Department of Surface and Plasma Science, Faculty of Mathematics and Physics, Charles University, V Holešovičkách 2, 180 00, Prague 8, Czech Republic
[c] Department of Physics, Computer Science and Mathematics, University of Modena and Reggio Emilia, 41125, Modena, Italy
[d] ELETTRA - Sincrotrone Trieste S.C.p.A., SS 14 - km 163,5, 34149, Basovizza, Trieste, Italy
[e] Istituto Nanoscienze (NANO-S3), Consiglio Nazionale delle Ricerche (CNR), Via G. Campi 213/a, Modena, 41125, Italy
[f] Centro H2-MORE, Univeristy of Modena and Reggio Emilia, 41125, Modena, Italy
[g] Graz University of Technology, Institute for Inorganic Chemistry, Stremayrgasse 9, 8010, Graz, Austria

HIGHLIGHTS

- A unitised electrochemical cell for operando X-Ray-based analyses is presented.
- It be used for studying catalyst materials in fuel cells and electrolysers.
- X-Ray Absorption Spectroscopy, Small-Angle Scattering and electrochemistry can be combined.

GRAPHICAL ABSTRACT

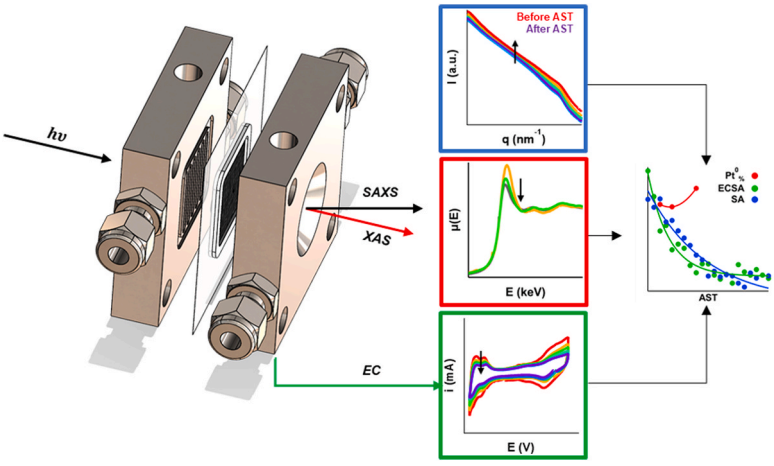

ARTICLE INFO

Keywords:
Operando
XAS
SAXS
PEMFC
PEMWE

ABSTRACT

Catalyst stability is a key issue in current electrochemical devices, such as fuel cells (FCs) and water electrolysers (WEs). While for FCs, the main degradation process limiting catalyst stability have been highlighted, a clear picture is still missing concerning WEs. In this framework, *in operando* analyses are essential to characterize catalyst degradation over time. As X-Rays constitute the perfect probe for studying catalytic materials, we here present a reversible electrochemical cell designed for *operando* X-Ray Absorption Spectroscopy and Small and Wide Angle X-Ray Scattering analyses, which was used: (i) to study Pt/C catalyst degradation coupling the evolution of specific electrochemically active surface area (ECSA) with catalyst morphology, supported by the

* Corresponding author. Department of Engineering and Architecture, University of Trieste, Via A. Valerio 10/1, 34127, Trieste (TS), Italy.
E-mail address: marco.bogar@dia.units.it (M. Bogar).

https://doi.org/10.1016/j.jpowsour.2024.235070
Received 4 April 2024; Received in revised form 3 July 2024; Accepted 15 July 2024
Available online 20 July 2024

analysis of Pt oxidation state. As a result, an increase of particle (and particle cluster) size is connected to the diminishing of ECSA and to the changes in the fraction of metallic-to-oxidised Pt, underlying that changes mainly develop in the first 2000 cycles of applied stress tests. Finally, (ii) we introduce some preliminary results underlying the change in Ir oxidation state for a standard Ir/IrO_X catalyst material for WEs, showing as such a change is not sufficient to induce any remarkable morphological variations within 500 cycles of stress tests.

1. Introduction

To support the transition from fossil fuels to (more) sustainable energy economies, green hydrogen is one of the most effective energy vectors to be employed for energy storage, thanks to its high energy density and to the absence of greenhouse gases emissions when obtained via water electrolysis. Its use is particularly appealing in the decarbonization of the so-called hard to abate sectors, such as the heavy industry and the maritime. Nonetheless, the production of cost-effective and efficient electrolysers and fuel cell systems is fundamental for promoting the spread of green hydrogen generation and use.

To date, low temperature Proton Exchange Membrane Fuel Cells (PEMFC) are the most mature technology available on the market, as they are already used in the automotive and the transportation sectors [1]. However, PEM technology still suffers of some limitations, which are mainly related to the need in reducing their costs while maintaining good stability over time [2–5]. The same issues are currently affecting Proton Exchange Membrane Water Electrolysers (PEMWE). Having the same architecture as PEMFC, their technological development and market diffusion could benefit if stability of the components of the Membrane Electrode Assembly (MEA) would be improved, reducing initial investment costs and increasing a lifetime [6–10]. While costs are mainly related to the platinum-group precious metals (such as iridium and ruthenium), used as a catalyst for the Oxygen Evolution Reaction (OER) [11,12], reduction of catalyst stability over time is due to the high operating potentials at which water electrolyzers need to be run, inducing enhanced coarsening in the MEA [6]. In all of these cases, it is evident as improvements can still be made in optimizing the design of the MEAs to be used for PEM technologies. In this framework, important insights were obtained moving from *ex situ,* to *in situ* and *in operando* analysis [13], where variations in device performances can be linked to the evolution of the main electrochemical parameters recorded.

Because of the plethora of possible events which were theorized taking place within the MEA during fuel cell operation, electrochemical analyses have not been decisive yet for fully depicting catalyst degradation *in operando* conditions, and important insights could only be achieved by means of *in situ*, and (more recently) *in operando* analysis carried out at synchrotron research infrastructure facilities. In fact, X-Ray Absorption Spectroscopy (XAS) has been already used to investigate the reaction kinetics of catalyst materials for PEMFC in catalyst formulations for commercial materials [14–17]. In addition, important results were also achieved concerning the stability of a novel low-Pt content catalyst materials, depending on the used support [18]. In parallel, the use of Small Angle X-Ray Scattering (SAXS) in combination with XAS [19] or with X-Ray Diffraction (XRD) [20,21] was recently used to depict the morphological evolution of catalyst materials at the nanoscale, allowing to observe and distinguish among particle coalescence and Ostwald ripening, two of the main phenomena known to affect catalyst stability and previously observed only through *in situ* investigation techniques [22–27].

However, designing a complete working electrochemical cell dedicated to *in operando* measurements at synchrotron facilities is not straightforward, due to the peculiar design needed to both guarantee satisfying performances and allowing the presence of windows for the X-Ray path, without jeopardizing the delicate equilibrium of the operating fuel cell. Ideally thermal, electrical and reactant transport pathways should not be interrupted, rendering part of catalyst layer subjected to signal acquisition representative. To date, and to the best of our knowledge, only few electrochemical cells were realized for such a kind of analysis: in example, Martinez and co-workers [28] developed and electrochemical cell for monitoring the aging of the electrolyte layer in PEMFCs, or by Martens et al. [29], who developed an electrochemical cell allowing to characterize the catalyst material along the MEA cross-section. Concerning electrolysers, such a kind of analysis is still at the early stages, and, to the best of our knowledge only few *in situ* [30] and *in operando* [31,32] analysis have been reported. In this context, basing on a standard design already developed in the past [33,34], we developed a novel reversible universal electrochemical cell able to operate both as PEM (or Anion Exchange Membrane, AEM) fuel cell for investigating the effects of the HOR and the ORR, as well as opening the possibilities to shed light on the processes underneath the Hydrogen Evolution Reaction (HER) and the OER in PEM (or AEM) water electrolysers (WE). In this extent, (i) the main aspects related to the cell design will be discussed at first, while (ii) in the second part of the paper the cell will be used to observe the chemical and morphological evolution of a standard Pt/C catalyst material for PEMFCs by means of XAS and SAXS, respectively. Finally, (iii) preliminary analysis on PEMWE will be reporting an oxidation phenomenon similar to the one recently reported by Diklić and co-workers [31].

2. Experimental

2.1. The reversible unitised electrochemical cell

The presented electrochemical cell (redesigned from a previous prototype [18]) was realized for investigating chemical and morphological evolution related to catalyst and support degradation in PEMFCs and WEs. In Fig. 1a an exploded 3D sketch of the cell is shown: the MEA (1, active area up to 2 cm × 2 cm) is sandwiched in between two titanium-made bipolar plates (2). Titanium was selected due to its excellent electrical and thermal conduction, but also because of its chemical stability when the cell is operated as FC or WE in both acidic and alkaline media. The bipolar plates host the flow field (3, pitch 0.8 mm), the electrical connections (4), the cartridge used for heating the cell (5), and the thermocouples for controlling the cell temperature (6). Two silicone gaskets (7) are used to seal the MEA, while reactants and reaction products are fed and drained by four lateral pipes (8). At the centre of the flow field, in the channel for reactants distribution, a slit (0.8 mm × 1 mm) is drilled to allow beam passage across the cell, thus probing the MEA in the same operational conditions without compromising its performance. Kapton windows (DuPont, thickness: 13 μm, 5 mm in diameter) are glued to the bipolar plates to seal entrance and exit slits by using an ethyl 2-cyanoacrylate-based glue. Kapton is characterized by excellent mechanical and thermal stability, as well as to favourable transparency to hard X-Rays. The bipolar plates have an asymmetrical design which allows them to be used for XAS measurements carried out either in transmission or fluorescence mode (Fig. 1b), as well as to record Wide Angle X-ray Scattering (WAXS) patterns up to 45° (Fig. 1c). A portable control station (P&ID represented in Fig. S1 in Supplementary Materials) is used for control of operating conditions (temperature, relative humidity, and gases flow rate) of the fuel cell.

2.2. MEA preparation

With the aim of investigating the effects on the ORR for PEMFC, two twin MEAs were prepared. The MEAs were composed by a self-made

Catalyst Coated Membrane (CCM) loaded with a benchmark Pt/Vulcan catalyst layer for the cathode electrode. The CCMs were prepared by ultrasonic spraying of a catalyst ink on the surface of an ionomeric membrane (Nafion® NR-211, FuelCellStore) by means of a CNC controlled system (ExactaCoat, Sono-Tek), as detailed in previous works [35,36]: Pt/C catalyst particles (Pt on Vulcan XC-72R, 40 %, FuelCellStore), ionomer dispersion D521 (5 % 1100 EW, FuelCellStore) and isopropanol/acetone solvent (1:1 ratio) were ultrasonically mixed forming the catalyst ink, characterized by a ionomer-to-carbon ratio equal to 0.6 [35]. The membrane was secured on a hot-bed (60 °C) during spraying process. Catalyst load on the cathode electrode was set to 0.4 $mg_{Pt}\cdot cm^{-2}$ for XAS analysis, and to 0.8 $mg_{Pt}\cdot cm^{-2}$ for SAXS ones. The higher load used in SAXS measurements were selected for guaranteeing catalyst detectability. Concerning the anode electrode, Pt was used (loading: 0.05 $mg_{Pt}\cdot cm^{2}$) for the MEA measured by SAXS, whereas for XAS measurements it was replaced with Pd (loading: 0.2 $mg_{Pd}\cdot cm^{2}$) in order to avoid any contamination of the XAS signal from the catalyst layer deposited on the anode side. Pd based catalyst demonstrate similar HOR performance as Pt (Fig. S2), can be used for XAS experiments with operando setup. The CCMs were sandwiched between two commercial Gas Diffusion Layers (GDLs, H24C5, Freudenberg).

When focusing on the OER for PEMWE, a couple of twin MEAs were loaded with benchmark Ir/IrO_X catalyst at the anode (1 $mg_{Ir}\cdot cm^{-2}$) prepared by the Meyer Rod technique. For the cathode electrode, the aforementioned Pt/Vulcan catalyst (0.5 $mg_{Pt}\cdot cm^{-2}$) was used for SAXS analysis and the Pd/Vulcan catalyst (0.5 $mg_{Pd}\cdot cm^{-2}$) was used for XAS analysis. A commercial carbon-based GDL (H24C5, Freudenberg) was used at the cathode, while a titanium fibre felt (FuelCellStore) was used at the anode.

2.3. X-Ray Absorption Spectroscopy

Pt and Ir XAS spectra at the L_3-edges were collected in transmission mode at the XAFS beamline of the ELETTRA synchrotron [37], using ionization chambers as detectors, a fixed exit Si (111) monochromator, and a beam size of 0.6 × 0.5 mm (the beamline has unfocused beam, whose dimension on the sample can be tuned as needed). For all samples, energy calibration was accomplished by collecting simultaneously a spectrum of a metallic reference placed in a second experimental chamber after the sample and after the second ionization chamber, with the position of the first inflection point settled to 11215.0 and 11564.0 eV for Ir and Pt, respectively. Spectra of reference compounds were either already available from previous experiments at XAFS beamline [18], or provided by the beamline database. All spectra were collected with a variable energy step as a function of the energy: 5 eV-steps in the first 200 eV of the spectrum, 0.2 eV-step in the XANES region, and a k-constant step of 0.03 $Å^{-1}$ in the EXAFS region for *ex-situ* measurements and of 0.05 $Å^{-1}$ for spectra collected *in operando*. The XANES spectra of samples and model compounds were normalized with respect to the background of the curve using the Athena software [38]. For the pristine Pt spectrum collected *ex-situ,* EXAFS refinement was also performed. Signal was extracted using Athena, Fourier transformed with a Hanning window in the k range 3 ÷ 11 $Å^{-1}$ and quantitative analysis was carried out using the Artemis software (Demeter 0.9.25 package) [39]. The shells for metallic Pt have been calculated using the crystallographic data of Wyckoff [40]. The XANES spectra collected *in operando* have been analysed through linear combination fitting (LCF) of spectra from the reference compounds, using the Athena software, to estimate the average oxidation state.

2.4. Small Angle X-Ray Scattering

SAXS measurements were conducted in transmission mode and *in operando* conditions, at room temperature and pressure on the Austrian SAXS beamline at the ELETTRA synchrotron in Trieste, Italy [41], using a wavelength of 0.77 Å (16 keV), a beam size of 0.8 × 0.5 mm and with a sample-to-detector distance set to 222.57 cm. A 2D pixel detector (Pilatus3 1 M, Dectris) was used to record scattering which were radially integrated by means of the SAXSDOG [42] software. Silver behenate was used as a calibrant. Resulting scattering patterns were analysed within the q-range from 0.097 nm^{-1} to 6.376 nm^{-1}. IGOR Pro software (IGOR Pro 7.0.8.1, Wavemetrics) was used for data reduction and fitting. The pattern record from the empty cell was used for background subtraction, while least square fitting was performed by using the analytical model presented in a previous work [43]: here, catalyst nanoparticles are modelled as a product of a form factor by a structure factor, $I(q) \propto I_P \bullet P(D_P, \sigma_P, q) \bullet S(D_f, \xi, q)$. As shown in our previous work [43] (due to the masking effect introduced by the presence of the GDL, and in agreement with the approximations presented by Gommes and co-workers [44]), the cross-cross-correlation term was neglected from the model, allowing to use an analytical model for the form factor. As a form factor a set of spheres following the Schulz distribution was used [45] to retrieve particle size distribution expressed in terms of forwarded scattering probability (I_P), mean particle size (D_P), and its standard deviation (σ_P). As a structure factor, particle clusters were modelled via the fractal model developed by Teixeira [46], characterized by the fractal dimension (D_f) related to the morphology of the cluster shape, and by the cut-off distance (ξ), describing the behaviour of the pair correlation function for larger distances than the size of a catalyst nanoparticle. Such a distance can be related to the average cluster size and by means of

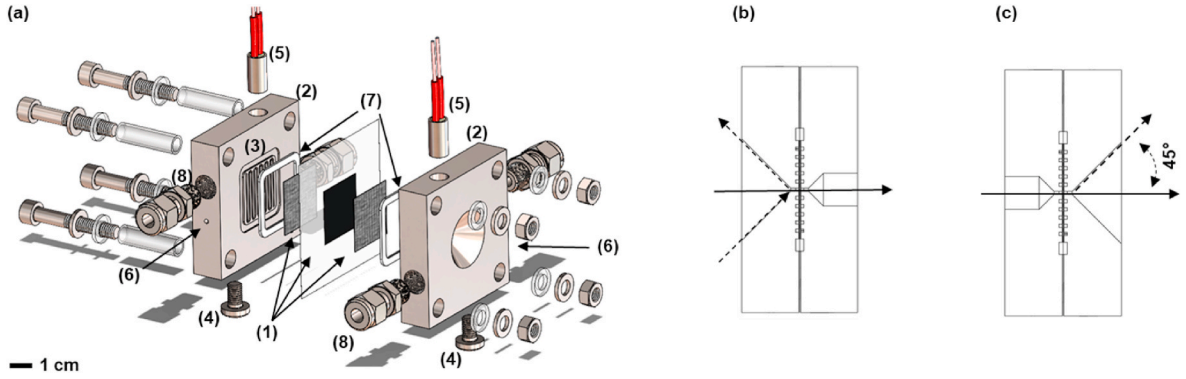

Fig. 1. The electrochemical cell. (a) 3D exploded sketch of the electrochemical cell; here the main components are marked by numbers: (1) MEA, (2) the bipolar plates, (3) the flow field, (4) threaded holes for electrical connections, (5) holes for hosting cartridge heaters, (6) holes for hosting the thermocouples, (7) silicone gaskets, (8) inlets and outlets for reactants and products of reaction. Kapton windows are too small to be resolved in this drawing. Exemplative sketches for cell use in (b) XAS and (c) Small and Wide Angle X-Ray Scattering (SWAXS) setups. Here, continuous lines represent configuration used for this work (transmission XAS and SAXS), dashed lines represent the possible setups with which the cell could be used (XAS performed in fluorescence mode and SWAXS), but not employed for this work.

the calculated radius of gyration $R_g^2 = \xi^2 D_f(D_f+1)/2$ [47]. Catalyst specific surface area, SA was further calculated as $SA = \langle A\rangle / \rho\langle V\rangle$ [19,43], where $\langle A\rangle$ and $\langle V\rangle$ respectively represent the average surface and volume of the catalyst nanoparticles, calculated as the second and third moment of the Schultz probability distribution function [48,49]: $\langle A\rangle = 4\pi \int_0^{R_{max}} f(r) r^2 dr$, $\langle V\rangle = \frac{4\pi}{3} \int_0^{R_{max}} f(r) r^3 dr$. The Vulcan support was modelled by means of the Debye-Anderson-Brumberger (DAB) form factor [50,51] by keeping the value of correlation length fixed to 36.07 nm, as previously done [43]. The GDLs are represented by a power law, and, for patterns not recorded by MEAs in dry conditions, the ionomer peak of Nafion was modelled as a Voigt peak [52–56]. The Pt/Vulcan loading at the anode electrode was selected to be 16 times lower than the loading at the cathode (anode: 0.05 $mg_{Pt}{\cdot}cm^{-2}$, cathode: 0.8 $mg_{Pt}{\cdot}\ cm^{-2}$) in order to be able to consider negligible the contribution given by the catalyst particles at the anode side (and due to the fact that particles at the anode are not supposed to evolve as fast as the particle population at the cathode, that the forwarded scattering pattern is stronger for larger, aged, particles).

2.5. In operando SAXS and XAS electrochemical measurements

Measurements by operating the cell as a fuel cell. In this configuration, MEAs were subjected to the same protocol in both *in operando* SAXS and XAS analysis. At first, the status of the sample was recorded (i) in dry conditions. Then, (ii) a conditioning protocol was run to hydrate the MEA and warming up the cell: cell temperature (T_{cell}) was set to 80 °C, while humidified N_2 (relative humidity, RH: 100 %, flow rate, Φ: 50 ml/min) was flown through both of the electrodes for 60 minutes. SAXS patterns were continuously recorded (one pattern every 20 minutes), for monitoring the evolution of the features representative of Nafion, checking any possible overlapping with the footprint characterizing catalyst nanoparticles. Due to the fact that no chemical changes are expected to be detected in this step, only one XAS spectra was recoded at the end of conditioning. Then, the MEAs undergo a (iii) break-in procedure, for activating the catalyst layer and checking the operative conditions of the FC: cell temperature was kept at 80 °C, while H_2 (20 ml/min) and O_2 (20 ml/min) were respectively flown at the anode and cathode electrodes. Chrono-amperometry was run for at least 120 minutes, by applying a difference of potential of 0.4 V at the cell by means of a potentiostat (SP-240, Biologic); the recorded current is shown in Fig. S3a. Both SAXS patterns and XAS spectra were continuously recorded, collecting a single measurement (pattern or spectrum), every 20 minutes. Finally, (iv) Accelerated Stress Tests (AST) [57] were applied to induce Pt oxidation and accelerate carbon-based support electrochemical corrosion, simulating a cathode voltage surge in fuel cell start-up/shut-down operation: cyclic voltammetry was run from 1.0 to 1.5 V at the sweep rate of 500 mV s^{-1} for 5000 cycles. During *in operando* SAXS measurements, one scattering pattern was recorded every 250 cycles. With the same frequency, a Potentiostatic Electrochemical Impedance Spectroscopy (PEIS) spectrum was recorded in the frequency range of 1 ÷ 100 kHz, at the potential of 0.85 V, together with three additional CV ranging from 0.05 to 1.0 V at the scan rates of 20, 50, and 100 mV s^{-1}. From voltammograms the specific Electrochemically active Surface Area (ECSA) was calculated as the ratio among the underpotential deposited hydrogen charge (Q (H_{UPD}), obtained by integrating the current values within the hydrogen desorption region) and the product of the hydrogen adsorption charge on a smooth Pt electrode (C = 210 μC cm^{-2}) by the mass of the catalyst loading per unit area (m_{Pt} = 0.8 $mg{\cdot}cm^{-2}$): $ECSA = Q(H_{UPD}) / (C \bullet m_{Pt})$. Due to temporal constrains, *in operando* XAS analysis were limited to 2000 cycles, and XAS spectra were recorded before starting AST (under potential of 0.4 V), and at 500, 1000, and 2000 cycles (under oxidative potential, 1.0 V, Fig. S4).

Measurements by operating the cell as a water electrolyser. With the aim of studying chemical as well as structural changes of the Ir/IrO_X catalyst under operation in MEA we developed two different protocols for XAS and SAXS, respectively. A first XAS spectrum was recorded *ex situ*, to depict the state of the MEA in pristine conditions. Afterwards, with the aim of understanding of how catalyst chemical composition varies during operation, *in operando* analysis were performed. Deionized water was flown in the cell (flow rate: 100 ml/min) for 60 minutes, with an operating cell temperature of 60 °C. Then, XAS spectra were recorded while running chrono-amperometry. A fixed potential was set across the cell starting from 1.1 V to 2.5 V, with a step of 0.1 V (Fig. S3b). For each potential step, after a waiting time of 10 minutes set to allow current stabilization, a XAS spectrum was recorded. According to the results thus obtained, SAXS analysis were repeated on a twin sample, with the aim of investigating the presence of morphological variations in catalyst nanoparticles induced by the revealed change in oxidation state. The scattering pattern of the MEA was firstly recorded in pristine conditions. Afterwards, the MEA was hydrated by pumping deionized water (flow rate: 100 ml/min, cell temperature: 60 °C) for 60 minutes. A break-in procedure followed in order to activate the catalyst (chrono-potentiometry run for 30 minutes at a current value fixed to 0.2 A cm^{-2} at first, and later for 30 minutes at a current value set to 1 A cm^{-2}). Finally, AST were run for 500 cycles. Each cycle consisting in potential switching from 1.45 to 1.80 V; each potential was held for 25 seconds.

3. Results and discussion

The presented reversible unitised electrochemical cell was used at first as a fuel cell, to investigate time-resolved degradation of the catalyst layer of a MEA undergoing AST by combining electrochemical, morphological, and spectroscopic analyses. In pristine conditions, the MEA is characterized by a scattering pattern which is mainly composed by a broad bump generated by the catalyst nanoparticles and a background with a constant slope due the presence of both the catalyst support layer and the GDL (Fig. S5a). From least square fitting of the SAXS pattern from the MEA in pristine conditions, it was found as the particle population is characterized by a mean particle diameter of 2.28 ± 0.02 nm (Fig. S5b), in agreement with previous analysis of us carried out on analogous MEAs [43]. Linear combination fitting of the absorption spectrum within the XANES region (Fig. S5c), revealed as the ratio among metallic-to-oxidised Pt (Pt^0/Pt^{2+}) is equal to 89-to-11 % (±3 %) whereas least square fitting of the EXAFS region (Figs. S5d and S5e) allowed to determine an average Pt–Pt bond length of 2.748 ± 0.003 Å, in line with other results provided in literature [19,58–61] (Fig. S5f). During conditioning and break-in stages, no remarkable variations in catalyst morphology was detected, and the only differences noticeable in the scattering patters are due to the hydration of the Nafion electrolyte upon water uptake and hydration, which can be related to the rise in intensity of the ionomer peak around 2 nm^{-1} (Fig. S6a). As extensively reported in literature [62–65], the increase in the intensity of the ionomer peak is related to the growth in size of the ionomeric regions, which are dedicated in sustaining the proton transport. As a control, the same conditioning procedure was repeated *in situ*, on a bare Nafion membrane (Fig. S7), where Nafion hydration could be observed in detail. On contrary, from the comparison of the XAS spectra recorded before and after the break-in operation, a slight variation was detected in the XANES white line intensity (Fig. S6b): the ratio among metallic-to-oxidised Pt was found equal to 95-to-5 % (±4 %) after break-in, which can be reconducted to the already known polishing Pt surface from oxides formed during the fabrication process. Nonetheless, despite a fully-reduced Pt was expected (due to the 0.4 V potential applied), it worth to mention that the existence of oxidised Pt under reductive potentials may be attributed to Pt particles detached from triple phase boundary regions, and therefore not participating in the electrochemical reaction.

Afterwards, AST were started: recorded voltammograms, SAXS patterns, and XAS spectra are shown in Fig. 2. Voltammograms reveal the

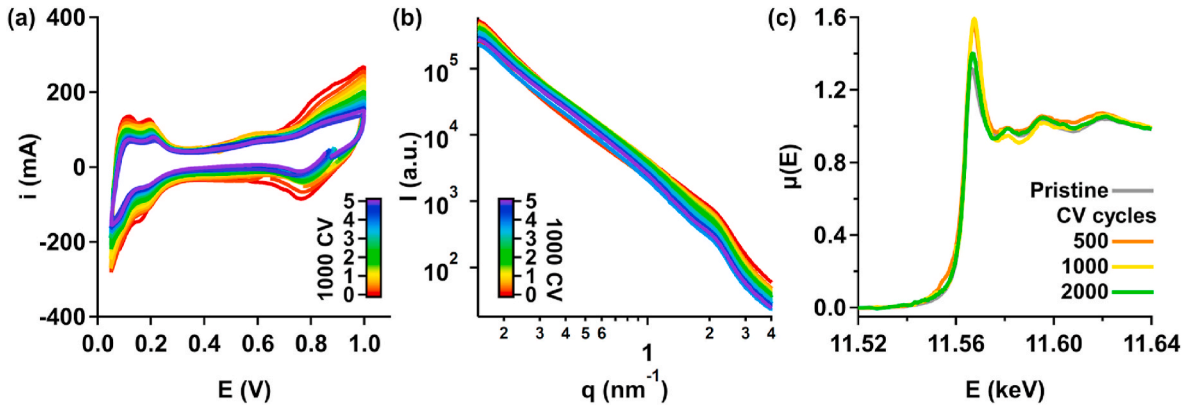

Fig. 2. *In operando* SAXS and XAS analysis. Time resolved evolution of (a) cyclic voltammograms, (b) SAXS patterns, and (c) XAS spectra recorded during *in operando* experiments. Traces identified by the number 0 indicate the state of the MEA before starting the AST, after break-in procedure was run.

typical shape corresponding to polycrystalline platinum oxidation and reduction regions, separated by the so-called double layer one. As expected, due to the high potential values at which the catalyst layer was subjected under AST, enhanced coarsening of the catalyst particles, particle detachment, and carbon support corrosion are known to concur [66] in a general reduction of the recorded currents in different parts of the voltammogram (Fig. 2a). Current reduction is overall visible in regions characteristics of hydrogen absorption and desorption (0.05 ÷ 0.40 V), as well as in the regions of Pt oxidation and reduction (0.8 ÷ 1.0 V). Moreover, region of double layer capacitance charge/discharge (0.4 ÷ 0.6 V) also shows lower currents over AST cycling. Decrease of current linked to the Pt features can be a result of Pt particles coarsening or/and their detachment from the carbon support, whereas double layer current decrease may be a result of carbon corrosion. Contemporary, some variations can be spotted in the temporal evolution of SAXS scattering patterns (Fig. 2b), where the footprint generated by the population of catalyst nanoparticles shifts towards lower q-values, thus highlighting a general growth either of particle size and/or state of aggregation. To better highlight such a variation, scattering correlation length [67] was calculated over the q-range of interest (Fig. S8), due to its particular sensitivity to size variations it was used as a qualitative marker to monitor the degree of evolution of the particle population. Finally, by comparing XAS spectra evolution (Fig. 2c), the white line intensity varies over time (increasing at first to further decrease after 2000 CV cycles), addressing to changes in the metallic-to-oxidised Pt ratio, which will be discussed in the next paragraph.

Quantitative, in-depth analysis started from ECSA calculation: from an initial value of 29 m^2/g_{Pt}, ECSA was found to be reduced to 8.5 m^2/g_{Pt}, for a total percentage reduction equal to about 70 % (Fig. 3a). Moreover, ECSA reduction is mostly pronounced within the first 2000 CV cycles (when it reaches a value of 10.4 m^2/g_{Pt}), to later stabilize into a plateau until 5000 CV cycles, in agreement with the trend observed in

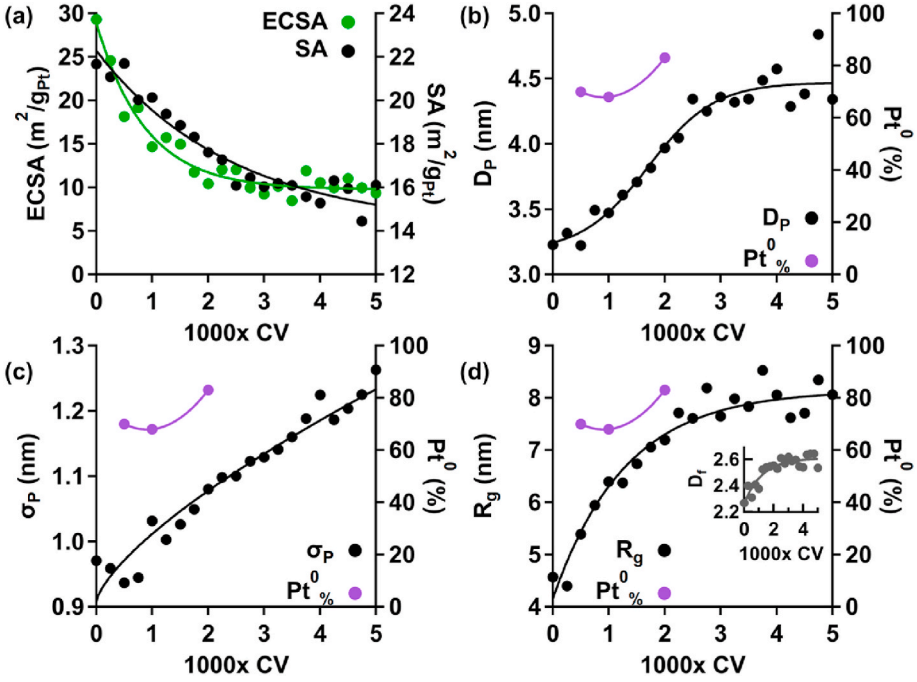

Fig. 3. Quantitative analysis. Time resolved evolution of (a) ECSA (calculated from the voltammograms shown in Fig. 2a) is compared with the evolution of SA (calculated from analytical fitting of SAXS patterns). Time resolved evolution of the main parameters composing the analytical model used to fit the scattering patterns shown in Fig. 2b: (b) mean particle diameter (D_P) and (c) standard deviation (σ_P) within the Schulz distribution, and (d) calculated radius of gyration (R_g), representative of the average cluster size. In (d), fractal dimension (D_f) is shown as an insert. In (b), (c), and (d), morphological parameters are compared with the chemical information retrieved by XAS, summarised by the evolution in the measured percentage of metallic Pt. Fill lines are a guide for the eye only. The time resolved analysis of all of the parameters composing the MEA is shown in Fig. S10.

the XANES spectra. In fact, within the first 500 and 1000 CV cycles, the amount of Pt^{2+} in the sample was observed rising up to 30 % (±1 %), and 32 % (±1 %) respectively (increasing of the white line intensity; determined through LCF), whereas, after 2000 cycles, the amount of Pt^{2+} reduces to 17 % (±2 %), meaning that the electroactive Pt was roughly the half with respect to the first CV, matching well with the ECSA values reported in Fig. 3a. Higher amounts of oxidised Pt at early stages of AST is a result of application of highly positive (anodic) potentials (1 ÷ 1.5 V) to large amount of catalyst particles. As AST proceeds, two processes take place: enlargement of catalyst particles which is evident from decrease of SA (Fig. 3a) and detachment of catalyst particles from electrochemical pathways due to support corrosion. The result of the two processes is that lower amount of catalyst particles can participate in the reaction and, therefore, lower amount of Pt can be oxidised.

The aforementioned findings were found in agreement with observed morphological evolution. Being aware that evolution of Nafion morphology could introduce a change in the background (which could potentially affect fitting results), the hydration state of the MEA was checked by comparing the evolution of ionomer peak position retrieved via SAXS and membrane resistance recorded by means of PEIS (Fig. S9). Being the standard deviation value below 1 % for both quantities Nafion was considered being in stable conditions (at least during the measurement window), and the SAXS fit results were considered reliable. Under these premises, the focus was thus addressed to the evolution of catalyst morphology. In Fig. 3b and c the growth of mean particle diameter (D_P) and standard deviation (σ_P) are respectively shown: in agreement with previous studies of us, carried out on catalyst model systems [26] (as well as highlighted *in operando* conditions [20]), an initial slower growth in both quantities is followed by a sudden increase in the growth rate in between 750 and 1000 CV cycles, where we previously addressed as in such interval the leading degradation protocol switches from coarsening to Ostwald ripening [25–27]. Finally, in between 2000 and 3000 cycles particle growth stops and the evolution of mean particle diameter stabilizes to a plateau. Such behaviour was already observed on catalyst model systems [25], and in principle this trend agrees with ECSA evolution: at this stage catalyst particle population is formed by bigger particles, having a reduced surface-to-volume ratio. Thus, they are less active and consequently less prone to further degrade. Moreover, some particles could have detached from catalyst support, becoming electrochemically inactive and thus introducing a bias into the size distribution. This fact might be also supported by the more prolonged evolution of particle standard deviation from the mean value (Fig. 3c), which keeps evolving until the end of the stress test. Afterwards, from the form factor parameters, the SAXS specific surface area was calculated (Fig. 3a): from an initial starting value of 21.7 m^2/g_{Pt}, the specific surface area was found reducing to 15.6 m^2/g_{Pt}, equivalent to a reduction at about 70 %. Such a result was found in great agreement with both the evolution and the values provided by ECSA; some differences in absolute values were considered reasonable because representative of two different physical surfaces. Nonetheless, also in this case, the most pronounced variations take place within the first 2000 cycles, while the assessment to the plateau value evolves in between 2000 and 3000 cycles. Finally, from the evolution of the structure factor parameters, the average cluster size (Fig. 3d) grows in agreement with the evolution of particle diameter, and an increase in cluster compactness (Fig. 3d, insert) can be related to the (small) increase of the fractal dimension within the first 1000 CV cycles. The evolution of the other parameters composing the model is shown in Fig. S10.

Then, the cell was set up to be used as a PEMWE. To study the effects of high anodic potential on the chemical state of the catalyst, *in operando* step-like chrono-amperometry was started from 1.0 V with potential steps of 0.1 V (Fig. S11a). As a result, no modifications were detected up to 1.4 V (spectra are overlapping with the pristine one). Then, a slight Ir oxidation was spotted as a shift towards higher energies of the high energy side of the main peak of Ir L_3-edge spectra; this transition happened when the applied difference of potential was between 1.5 and 1.6 V (Fig. 4a), but for larger potentials all the spectra show no further variations up to 2.4 V. The aforementioned transition result is very similar to that recently reported by Diklić and co-workers [31] and seems to be also fully reversible, as the spectrum collected after having run the electrolyser overnight perfectly overlaps the spectrum recorded in pristine conditions. By comparing the results here shown with the ones presented by Diklić et al. [31], a curve showing the differences of the spectra ($\Delta\mu$) collected above 1.6 V and below 1.4 V was calculated (Fig. 4b). Apart from a shift of 2.3 eV towards higher energies (maybe due to the different reference materials used for energy calibration), the amplitude of the obtained curve seems to fall in the middle of that of IrO_X *AS* and IrO_X *HT* samples reported by Diklić and co-workers [31]. Finally, with the aim of investigating if any morphological variations were also induced, SAXS patterns were recorded *in operando* conditions, while AST (consisting in potential switching among 1.45–1.80 V, in concordance with XAS results which suggest change of oxidation states of Ir) were run. The recorded scattering patterns are shown in Fig. S11b: here only slight variations in proximity of 1 nm^{-1} are detectable and, after fitting the displayed patterns, no clear morphological evolution can be highlighted. In fact, the most relevant phenomenon detectable is the continuous hydration of Nafion, represented by the shift of the ionomer peak towards lower q-values (q_{IP}, Fig. 4c). In parallel, catalyst nanoparticle evolution, if present, appears to be at its early stages, as the evolution of the mean particle diameter (D_P, Fig. 4c) shows a slightly increasing trend, and its standard deviation values (σ_P, Fig. 4c) starts shrinking. Nonetheless, the recorded variations are quite small and longer analysis would be required to highlight a clear trend.

4. Conclusions

With this work we have presented a portable and reliable setup, coupled with a solid methodology for combining *in operando* chemical, electrochemical, and morphological characterization for catalyst materials for PEM fuel cells and water electrolysers. The electrochemical cell was firstly used to depict degradation of a standard Pt/C catalyst material undergoing AST for fuel cell. After monitoring the state of the MEA during the stages of conditioning and break-in (used to properly humidify the membrane and activating the catalyst), AST were applied to induce catalyst oxidation and accelerate carbon-based support electrochemical corrosion by applying cyclic voltammetry from 1.0 to 1.5 V for 5000 cycles. Results from data analysis allowed to connect reduction in ECSA to morphological parameters obtained from SAXS (mean particle diameter and standard deviation, aggregation size and type, and specific surface area). XAS analysis allowed to support the comparison and provide a complementary point of view on the chemical state of Pt (quantifying the ratio among metallic-to-oxidised Pt). Afterwards, the cell was used to test *in operando* the stability of Ir/IrO_X catalyst material for water electrolyser. Here, XAS revealed the formation of Ir oxide when a potential of 1.5–1.6 V is applied to the electrochemical cell. According to that results, a dedicated AST was created for searching for morphological variations in the catalyst layer, but no remarkable variations could be highlighted within the temporal range in which the analysis was carried out. Nonetheless, this setup opens the possibilities for future analysis on new materials for both PEM fuel cells and water electrolysers.

CRediT authorship contribution statement

Marco Bogar: Writing – original draft, Visualization, Resources, Methodology, Investigation, Formal analysis, Data curation, Conceptualization. **Yurii Yakovlev:** Writing – original draft, Resources, Investigation, Formal analysis, Data curation, Conceptualization. **Simone Pollastri:** Writing – original draft, Methodology, Investigation, Formal analysis, Data curation, Conceptualization. **Roberto Biagi:** Writing – review & editing. **Heinz Amenitsch:** Writing – review & editing,

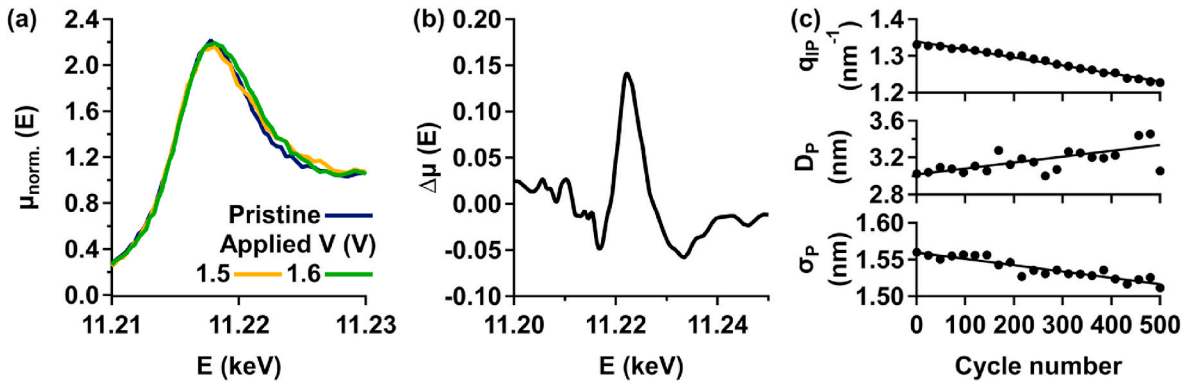

Fig. 4. ***In operando*** **water electrolysis.** (a) The normalized XANES spectra collected *in operando* at the Ir L_3-edge recorded while running AST at the potentials of 1.5 and 1.6 V, are compared with the spectrum recorded *ex situ* in pristine conditions (The complete series is shown in Fig. S11a). (b) Difference of the spectra acquired above 1.6 V and below 1.4 V (Δμ). (c) Main results from fitting the scattering patterns represented in Fig. S11b, recorded *in operando* while running AST: position of the ionomer peak (q_{IP}), and mean catalyst particle size (D_P) and standard deviation (σ_P) within the Schulz distribution. The fill lines are a guide for the eye only.

Validation, Resources, Methodology, Conceptualization. **Rodolfo Taccani:** Supervision, Resources, Funding acquisition. **Iva Matolínová:** Writing – review & editing, Supervision, Resources, Funding acquisition, Conceptualization.

Declaration of competing interest

The authors declare that they have no known competing financial interests or personal relationships that could have appeared to influence the work reported in this paper.

Data availability

Data will be made available on request.

Acknowledgments

All of the authors acknowledge the CERIC-ERIC Consortium for the access to experimental facilities and the financial support (proposal 20222217 scheduled at the SAXS beamline). Data at the XAFS beamline were collected during the experiment proposal 20220525. This work was supported by the project "The Energy Conversion and Storage", funded as project No. CZ.02.01.01/00/22_008/0004617 by Programme Johannes Amos Comenius, call Excellent Research, Ministry of Education, Youth and Sports of the Czech Republic. M.B. and R.T. acknowledge the financial support from the project sHYpS (sustainable HYdrogen powered Shipping, Horizon Europe call Horizon-CL5-2021-D5-01) and the Italian Operative Program for Research and Innovation 2014–2020 provided by the Italian Ministry of University and Research. S.P. also acknowledge Dr. Luca Olivi and Riccardo Grisonich for their help during the experiment at XAFS.

Appendix A. Supplementary data

Supplementary data to this article can be found online at https://doi.org/10.1016/j.jpowsour.2024.235070.

References

[1] A.N. Mancino, C. Menale, F. Vellucci, M. Pasquali, R. Bubbico, PEM fuel cell applications in road transport, Energies 16 (17) (2023), https://doi.org/10.3390/en16176129.
[2] Y. Wang, D.F. Ruiz Diaz, K.S. Chen, Z. Wang, X.C. Adroher, Materials, technological status, and fundamentals of PEM fuel cells – a review, Mater. Today 32 (February) (2020) 178–203, https://doi.org/10.1016/j.mattod.2019.06.005.
[3] B.G. Pollet, S.S. Kocha, I. Staffell, Current status of automotive fuel cells for sustainable transport, Curr. Opin. Electrochem. 16 (2019) 90–95, https://doi.org/10.1016/j.coelec.2019.04.021.
[4] H. Li, et al., Pt-based oxygen reduction reaction catalysts in proton exchange membrane fuel cells: controllable preparation and structural design of catalytic layer, Nanomaterials 12 (23) (2022), https://doi.org/10.3390/nano12234173.
[5] E. Zhu, et al., Stability of platinum-group-metal-based electrocatalysts in proton exchange membrane fuel cells, Adv. Funct. Mater. 32 (30) (2022) 1–21, https://doi.org/10.1002/adfm.202203883.
[6] F.N. Khatib, et al., Material degradation of components in polymer electrolyte membrane (PEM)electrolytic cell and mitigation mechanisms: a review, Renew. Sustain. Energy Rev. 111 (March) (2019) 1–14, https://doi.org/10.1016/j.rser.2019.05.007.
[7] A. Bazarah, et al., Factors influencing the performance and durability of polymer electrolyte membrane water electrolyzer: a review, Int. J. Hydrogen Energy 47 (85) (2022) 35976–35989, https://doi.org/10.1016/j.ijhydene.2022.08.180.
[8] A. Makhsoos, M. Kandidayeni, B.G. Pollet, L. Boulon, A perspective on increasing the efficiency of proton exchange membrane water electrolyzers– a review, Int. J. Hydrogen Energy 48 (41) (May 2023) 15341–15370, https://doi.org/10.1016/j.ijhydene.2023.01.048.
[9] P.L. Cabot, M.V. Martínez-Huerta, F. Alcaide, Advanced supports for noble metal catalysts in proton exchange membrane water electrolysers: a review, Johnson Matthey Technol. Rev. 67 (3) (2023) 249–265, https://doi.org/10.1595/205651323X16648726195503.
[10] Z. Zeng, et al., Degradation mechanisms in advanced MEAs for PEM water electrolyzers fabricated by reactive spray deposition technology, J. Electrochem. Soc. 169 (5) (May 2022) 054536, https://doi.org/10.1149/1945-7111/ac7170.
[11] E. Antolini, Iridium as catalyst and cocatalyst for oxygen evolution/reduction in acidic polymer electrolyte membrane electrolyzers and fuel cells, ACS Catal. 4 (5) (2014) 1426–1440, https://doi.org/10.1021/cs4011875.
[12] T. Wang, X. Cao, L. Jiao, PEM water electrolysis for hydrogen production: fundamentals, advances, and prospects, Carbon Neutrality 1 (1) (2022) 1–19, https://doi.org/10.1007/s43979-022-00022-8.
[13] J. Shan, R. Lin, S. Xia, D. Liu, Q. Zhang, Local resolved investigation of PEMFC performance degradation mechanism during dynamic driving cycle, Int. J. Hydrogen Energy 41 (7) (2016) 4239–4250, https://doi.org/10.1016/j.ijhydene.2016.01.048.
[14] N. Ishiguro, et al., Operando time-resolved X-ray absorption fine structure study for surface events on a Pt 3 Co/C cathode catalyst in a polymer electrolyte fuel cell during voltage-operating processes, ACS Catal. 2 (7) (Jul. 2012) 1319–1330, https://doi.org/10.1021/cs300228p.
[15] N. Ishiguro, M. Tada, Structural kinetics of cathode events on polymer electrolyte fuel cell catalysts studied by operando time-resolved XAFS, Catal. Lett. 148 (6) (Jun. 2018) 1597–1609, https://doi.org/10.1007/s10562-018-2383-7.
[16] N. Ishiguro, et al., Rate enhancements in structural transformations of Pt-Co and Pt-Ni bimetallic cathode catalysts in polymer electrolyte fuel cells studied by in situ time-resolved X-ray absorption fine structure, J. Phys. Chem. C 118 (29) (Jul. 2014) 15874–15883, https://doi.org/10.1021/jp504738p.
[17] E. Berretti, et al., Experimental evidence of palladium dissolution in anodes for alkaline direct ethanol and formate fuel cells, Electrochim. Acta 418 (April) (2022) 140351, https://doi.org/10.1016/j.electacta.2022.140351.
[18] S. Pollastri, et al., Characterization of innovative Pt-ceria catalysts for PEMFC by means of ex-situ and operando X-Ray Absorption Spectroscopy, Int. J. Hydrogen Energy 47 (14) (2022) 8799–8810, https://doi.org/10.1016/j.ijhydene.2021.12.241.
[19] M. Povia, et al., Combining SAXS and XAS to study the operando degradation of carbon-supported Pt-nanoparticle fuel cell catalysts, ACS Catal. 8 (8) (2018) 7000–7015, https://doi.org/10.1021/acscatal.8b01321.
[20] I. Martens, R. Chattot, J. Drnec, Decoupling catalyst aggregation, ripening, and coalescence processes inside operating fuel cells, J. Power Sources 521 (Feb. 2022) 230851, https://doi.org/10.1016/j.jpowsour.2021.230851.
[21] J. Schröder, et al., Tracking the catalyst layer depth-dependent electrochemical degradation of a bimodal Pt/C fuel cell catalyst: a combined operando small- and

wide-angle X-ray scattering study, ACS Catal. 12 (3) (2022) 2077–2085, https://doi.org/10.1021/acscatal.1c04365.
[22] J.A. Gilbert, et al., Pt catalyst degradation in aqueous and fuel cell environments studied via in-operando anomalous small-angle X-ray acattering, Electrochim. Acta 173 (May 2015) 223–234, https://doi.org/10.1016/j.electacta.2015.05.032.
[23] M. Ruge, et al., Structural reorganization of Pt(111) electrodes by electrochemical oxidation and reduction, J. Am. Chem. Soc. 139 (12) (Mar. 2017) 4532–4539, https://doi.org/10.1021/jacs.7b01039.
[24] I. Khalakhan, A. Choukourov, M. Vorokhta, P. Kúš, I. Matolínová, V. Matolín, In situ electrochemical AFM monitoring of the potential-dependent deterioration of platinum catalyst during potentiodynamic cycling, Ultramicroscopy 187 (2018) 64–70, https://doi.org/10.1016/j.ultramic.2018.01.015.
[25] I. Khalakhan, et al., Evolution of the PtNi bimetallic alloy fuel cell catalyst under simulated operational conditions, ACS Appl. Mater. Interfaces 12 (15) (2020) 17602–17610, https://doi.org/10.1021/acsami.0c02083.
[26] M. Bogar, I. Khalakhan, A. Gambitta, Y. Yakovlev, H. Amenitsch, In situ electrochemical grazing incidence small angle X-ray scattering: from the design of an electrochemical cell to an exemplary study of fuel cell catalyst degradation, J. Power Sources 477 (Nov) (2020), https://doi.org/10.1016/j.jpowsour.2020.229030.
[27] M. Bogar, et al., Interplay among dealloying, Ostwald ripening, and coalescence in PtXNi100-XBimetallic alloys under fuel-cell-related conditions, ACS Catal. 11 (18) (2021) 11360–11370, https://doi.org/10.1021/acscatal.1c01111.
[28] N. Martinez, et al., Heterogeneous nanostructural aging of fuel cell ionomer revealed by operando SAXS, ACS Appl. Energy Mater. 2 (5) (May 2019) 3071–3080, https://doi.org/10.1021/acsaem.8b02004.
[29] I. Martens, et al., X-ray transparent proton-exchange membrane fuel cell design for in situ wide and small angle scattering tomography, J. Power Sources 437 (Oct. 2019), https://doi.org/10.1016/j.jpowsour.2019.226906.
[30] D. Lebedev, et al., Atomically dispersed iridium on indium tin oxide efficiently catalyzes water oxidation, ACS Cent. Sci. 6 (7) (Jul. 2020) 1189–1198, https://doi.org/10.1021/acscentsci.0c00604.
[31] N. Diklić, et al., Surface Ir+5 formation as a universal prerequisite for O2 evolution on Ir oxides, ACS Catal. 13 (16) (2023) 11069–11079, https://doi.org/10.1021/acscatal.3c01448.
[32] T. Hrbek, P. Kúš, M.G. Rodríguez, V. Matolín, I. Matolínová, Operando X-ray photoelectron spectroscopy cell for water electrolysis: a complete picture of iridium electronic structure during oxygen evolution reaction, Int. J. Hydrogen Energy 57 (January) (2024) 187–197, https://doi.org/10.1016/j.ijhydene.2023.12.216.
[33] A. Parthasarathy, S. Srinivasan, A.J. Appleby, C.R. Martin, Electrode kinetics of oxygen reduction at carbon-supported and unsupported platinum microcrystallite/Nafion® interfaces, J. Electroanal. Chem. 339 (1–2) (1992) 101–121, https://doi.org/10.1016/0022-0728(92)80447-C.
[34] T. Binninger, et al., Electrochemical flow-cell setup for in situ X-ray investigations, J. Electrochem. Soc. 163 (10) (2016) H906–H912, https://doi.org/10.1149/2.0201610jes.
[35] Y.V. Yakovlev, et al., Ionomer content effect on charge and gas transport in the cathode catalyst layer of proton-exchange membrane fuel cells, J. Power Sources 490 (January) (2021), https://doi.org/10.1016/j.jpowsour.2021.229531.
[36] Y.V. Yakovlev, et al., Characterization of gas diffusion layer transport properties by limiting current approach, Electrochim. Acta 404 (2022) 139755, https://doi.org/10.1016/j.electacta.2021.139755.
[37] A. Di Cicco, et al., Novel XAFS capabilities at ELETTRA synchrotron light source, J. Phys. Conf. 190 (2009), https://doi.org/10.1088/1742-6596/190/1/012043.
[38] B. Ravel, M. Newville, ATHENA, artemis, hephaestus: data analysis for X-ray absorption spectroscopy using IFEFFIT, J. Synchrotron Radiat. 12 (4) (Jul. 2005) 537–541, https://doi.org/10.1107/S0909049505012719.
[39] M. Newville, IFEFFIT: interactive XAFS analysis and FEFF fitting [Online]. Available: http://astro.caltech.edu/, 2001.
[40] R.W.G. Wtckoff, Crystal structures volume 1. American Mineralogist Crystal Structure Database, 1963.
[41] H. Amenitsch, M. Rappolt, M. Kriechbaum, H. Mio, P. Laggner, S. Bernstorff, First performance assessment of the small-angle X-ray scattering beamline at ELETTRA, J. Synchrotron Radiat. 5 (3) (1998) 506–508, https://doi.org/10.1107/S090904959800137X.
[42] M. Burian, C. Meisenbichler, D. Naumenko, H. Amenitsch, SAXSDOG: open software for real-time azimuthal integration of 2D scattering images, J. Appl. Crystallogr. 55 (2022) 677–685, https://doi.org/10.1107/S1600576722003685.
[43] M. Bogar, et al., A small angle X-ray scattering approach for investigating fuel cell catalyst degradation for both ex situ and in operando analyses, Int. J. Hydrogen Energy 58 (January) (Mar. 2024) 1673–1681, https://doi.org/10.1016/j.ijhydene.2024.01.261.
[44] C.J. Gommes, T. Asset, J. Drnec, Small-angle scattering by supported nanoparticles: exact results and useful approximations, J. Appl. Crystallogr. 52 (3) (2019) 507–519, https://doi.org/10.1107/S1600576719003935.
[45] M. Kotlarchyk, R.B. Stephens, J.S. Huang, Study of Schultz distribution to model polydispersity of microemulsion droplets, J. Phys. Chem. 92 (6) (1988) 1533–1538, https://doi.org/10.1021/j100317a032.
[46] J. Teixeira, Small-angle scattering by fractal systems, J. Appl. Crystallogr. 21 (6) (1988) 781–785, https://doi.org/10.1107/S0021889888000263.
[47] C.M. Sorensen, G.M. Wang, Size distribution effect on the power law regime of the structure factor of fractal aggregates, Phys. Rev. E 60 (6) (1999) 7143–7148, https://doi.org/10.1103/PhysRevE.60.7143.
[48] J. Tillier, et al., Electrochemical flow-cell setup for in situ X-ray investigations, J. Electrochem. Soc. 163 (10) (2016) H913–H920, https://doi.org/10.1149/2.0211610jes.
[49] J.W. Bullard, Q. Jin, K.A. Snyder, How do specific surface area and particle size distribution change when granular media dissolve? Chem. Eng. J. 406 (Feb) (2021) https://doi.org/10.1016/j.cej.2020.127098.
[50] P. Debye, A.M. Bueche, Scattering by an inhomogeneous solid, J. Appl. Phys. 20 (6) (1949) 518–525, https://doi.org/10.1063/1.1698419.
[51] P. Debye, H.R. Anderson, H. Brumberger, Scattering by an inhomogeneous solid. II. the correlation function and its application, J. Appl. Phys. 28 (6) (1957) 679–683, https://doi.org/10.1063/1.1722830.
[52] B.H. Armstrong, Spectrum line profiles: the Voigt function, J. Quant. Spectrosc. Radiat. Transf. 7 (1) (Jan. 1967) 61–88, https://doi.org/10.1016/0022-4073(67)90057-X.
[53] E.E. Whiting, An empirical approximation to the Voigt profile, J. Quant. Spectrosc. Radiat. Transf. 8 (6) (1968) 1379–1384, https://doi.org/10.1016/0022-4073(68)90081-2.
[54] S.R. Drayson, Rapid computation of the Voigt profile, J. Quant. Spectrosc. Radiat. Transf. 16 (7) (1976) 611–614, https://doi.org/10.1016/0022-4073(76)90029-7.
[55] J. Humlíček, Optimized computation of the voigt and complex probability functions, J. Quant. Spectrosc. Radiat. Transf. 27 (4) (1982) 437–444, https://doi.org/10.1016/0022-4073(82)90078-4.
[56] F. Schreier, The Voigt and complex error function: a comparison of computational methods, J. Quant. Spectrosc. Radiat. Transf. 48 (5–6) (Nov. 1992) 743–762, https://doi.org/10.1016/0022-4073(92)90139-U.
[57] T. Abdel-Baset, et al., Fuel Cell Technical Team Roadmap, Jun. 2013, https://doi.org/10.2172/1220127.
[58] A.I. Frenkel, C.W. Hills, R.G. Nuzzo, A view from the inside: complexity in the atomic scale ordering of supported metal nanoparticles, J. Phys. Chem. B 105 (51) (Dec. 2001) 12689–12703, https://doi.org/10.1021/jp012769j.
[59] Y. Lei, J. Jelic, L.C. Nitsche, R. Meyer, J. Miller, Effect of particle size and adsorbates on the L3, L2 and L1 X-ray absorption near edge structure of supported Pt nanoparticles, Top. Catal. 54 (5–7) (2011) 334–348, https://doi.org/10.1007/s11244-011-9662-5.
[60] H.J. Wasserman, J.S. Vermaak, On the determination of the surface stress of copper and platinum, Surf. Sci. 32 (1) (1972) 168–174, https://doi.org/10.1016/0039-6028(72)90127-6.
[61] C. Solliard, M. Flueli, Surface stress and size effect on the lattice parameter in small particles of gold and platinum, Surf. Sci. 156 (PART 1) (1985) 487–494, https://doi.org/10.1016/0039-6028(85)90610-7.
[62] G. Gebel, O. Diat, Neutron and X-ray scattering: suitable tools for studying lonomer membranes, Fuel Cell. 5 (2) (Apr. 2005) 261–276, https://doi.org/10.1002/fuce.200400080.
[63] F. Xu, O. Diat, G. Gebel, A. Morin, Determination of transverse water concentration profile through MEA in a fuel cell using neutron scattering, J. Electrochem. Soc. 154 (12) (2007) B1389, https://doi.org/10.1149/1.2794287.
[64] J. Mališ, M. Paidar, T. Bystron, L. Brožová, A. Zhigunov, K. Bouzek, Changes in Nafion® 117 internal structure and related properties during exposure to elevated temperature and pressure in an aqueous environment, Electrochim. Acta 262 (Feb. 2018) 264–275, https://doi.org/10.1016/j.electacta.2018.01.011.
[65] L. Rubatat, G. Gebel, O. Diat, Fibrillar structure of Nafion: matching fourier and real space studies of corresponding films and solutions, Macromolecules 37 (20) (2004) 7772–7783, https://doi.org/10.1021/ma049683j.
[66] J.R. Varcoe, et al., Anion-exchange membranes in electrochemical energy systems, in: Energy and Environmental Science vol. 7, Royal Society of Chemistry, Oct. 01, 2014, pp. 3135–3191, https://doi.org/10.1039/c4ee01303d, 10.
[67] O. Glatter, Scattering Methods and Their Application in Colloid and Interface Science, Elsevier, 2018, https://doi.org/10.1016/c2016-0-04640-5.